COMMUNICATION

Check for updates

Light-driven dynamical tuning of the thermal conductivity in ferroelectrics†

Claudio Cazorla, [ID] [a] Sebastian Bichelmaier, [ID] [b] Carlos Escorihuela-Sayalero,[a] Jorge Íñiguez, [ID] [c,d] Jesús Carrete [ID] [b] and Riccardo Rurali [ID] *[e]

Dynamical tuning of the thermal conductivity in crystals, κ, is critical for thermal management applications, as well as for energy harvesting and the development of novel *phononic* devices able to perform logic operations with phonons. Such a desired κ control can be achieved in functional materials that experience large structural and phonon variations as a result of field-induced phase transformations. However, this approach is only practical within reduced temperature intervals containing zero-bias phase transition points, since otherwise the necessary driving fields become excessively large and the materials' performances are detrimentally affected. Here, based on first-principles calculations, we propose an alternative strategy for dynamically tuning κ that is operative over broad temperature conditions and realizable in a wide class of materials. By shining light on the archetypal perovskite oxide $KNbO_3$, we predict that ultrafast and reversible ferroelectric-to-paraelectric phase transitions are induced, yielding large and anisotropic κ variations (up to $\approx 30\%$ at T = 300 K). These light-induced thermal transport shifts can take place at temperatures spanning several hundreds of kelvin and are essentially the result of anharmonic effects affecting the phonon lifetimes.

1 Introduction

Current strategies to design materials with tailored thermal properties typically rely on the creation of structural inhomo-

[a]*Departament de Física, Universitat Politècnica de Catalunya, Campus Nord B4-B5, Barcelona 08034, Spain*
[b]*Institute of Materials Chemistry, TU Wien, A-1060 Vienna, Austria*
[c]*Materials Research and Technology Department, Luxembourg Institute of Science and Technology (LIST), Avenue des Hauts-Fourneaux 5, L-4362 Esch/Alzette, Luxembourg*
[d]*Department of Physics and Materials Science, University of Luxembourg, 41 Rue du Brill, L-4422 Belvaux, Luxembourg*
[e]*Institut de Ciència de Materials de Barcelona, ICMAB-CSIC, Campus UAB, 08193 Bellaterra, Spain. E-mail: rrurali@icmab.es*
†Electronic supplementary information (ESI) available. See DOI: **https://doi.org/10.1039/d4nr00100a**

geneities that scatter phonons and reduce the thermal conductivity (*e.g.*, lattice defects,[1] grain boundaries[2] and nanostructure surfaces[3]) and the engineering of periodic heterostructures (superlattices), in which wave interference induces the appearance of phonon frequency gaps.[4] These approaches, however, yield changes in the thermal properties of materials that are static and irreversible. Applications in the context of thermal management and energy harvesting, however, would benefit from the possibility of dynamically tuning the thermal conductivity of materials, κ.[5–7] Likewise, the design of phononic devices capable of performing logic operations with phonons, analogous to what their electronic counterparts do with charge carriers, may also be envisaged on the basis of the concept of active κ control.[8,9] Such a technological goal can be achieved, for instance, *via* strain[10] and chemical intercalation[11] in layered materials. However, these approaches appear to be rather impractical due to their long response times and complex setups.

A promising approach for dynamical κ tuning involves the exploitation of the effects of field-induced phase transitions on the thermal properties of functional materials like ferroelectric and magnetic crystals.[12–19] The ensuing electrophononic and magnetophononic effects are expected to lead to fast and dynamical manipulation of the heat carriers, thus yielding *à la carte* thermal properties for on-demand applications. Nevertheless, for these phononic phenomena to be practical, the operating conditions need to be close to the phase-transition points at zero bias since otherwise the required driving fields may grow unfeasibly large and the materials' performances may be seriously compromised owing to the presence of leakage/eddy currents and dielectric/magnetic losses.

On the other hand, the possibility of manipulating κ with light has received very little attention thus far, although some promising results in azobenzene-doped liquid crystals have been recently reported.[20] Light-driven control of the thermal conductivity could bypass some of the issues posed by the schemes described above (*e.g.*, application of large driving fields) and simplify the design of logic devices (*i.e.*, no need

for electrical contacts). Macroscopic light-driven phase transitions[21,22] involving collective phenomena such as electronic correlation, spin–lattice and charge–lattice couplings are especially appealing in this regard. Photoinduced phase transitions of these types have been reported for π-conjugated polymers,[23] transition metal oxides[24] and molecular crystals,[25] to cite a few examples. Remarkably, the dynamics of this class of light-driven phase transformation is ultrafast, in the scale of subpicoseconds for VO$_2$,[24] ≈1 ps for LaTe$_3$ [26] and 100–500 ps for inorganic perovskite nanocrystals.[27] More recently, ultrafast photo-driven control of the incipient ferroelectric KTaO$_3$ [28] and hydrogen-bonded ferroelectric crystals[29] has also been experimentally demonstrated, while it has been theoretically proposed that light-excited carriers can thermodynamically stabilize three-dimensional nanoscale polar structures in ferroelectric superlattices.[30]

In this Communication, we use predictive first-principles calculations to demonstrate dynamical tuning of the thermal conductivity in a ferroelectric perovskite oxide resulting from a reversible light-induced phase transition. These *photophononic* effects rely on large changes in phonon dispersion and phonon lifetimes caused by the suppression of ferroelectricity upon irradiation.[31] We explore this effect in the prototypical ferroelectric perovskite KNbO$_3$ (KNO), finding large and highly anisotropic κ variations (up to ≈30%) within a wide temperature interval spanning over several hundreds of kelvin. Our results can be qualitatively generalized to other ferroelectrics displaying displacive-like phase transitions such as BaTiO$_3$.[31]

2   Results and discussion

2.1   Light-induced phase transitions

At temperatures lower than 225 K, KNO exhibits a non-centrosymmetric rhombohedral $R3m$ phase with electric polarization oriented along the pseudocubic direction [111]. According to our first-principles calculations based on density functional theory (for DFT calculations, see Methods), this structure is characterized by a lattice parameter of 4.034 Å, a rhombohedral angle of 89.89° and a ferroelectric polarization of $P =$ 35.05 μC cm^{-2}. These results compare notably well with the corresponding experimental values of 4.016 Å, 89.83° and 30–40 μC cm^{-2}, respectively.[32–34] Upon (above-bandgap) light irradiation, some electrons are photoexcited and promoted from the valence to the conduction band, where they can move more freely and become delocalized throughout the crystal. These carriers turn out to screen the long-range dipole–dipole interactions that sustain polar order in the rhombohedral phase.[31,35] As a consequence, the nonpolar cubic phase $Pm\bar{3}m$, which under dark conditions is only stable at temperatures $T \geq$ 703 K,[32] can potentially become the new ground state (Fig. 1).

In particular, our zero-temperature DFT calculations show that the nonpolar $Pm\bar{3}m$ phase becomes stable at photoexcited electron densities of $n > \bar{n} = 2.69 \times 10^{21}$ cm^{-3}. This effect is illustrated in Fig. 2 where we plot the phonon dispersion of
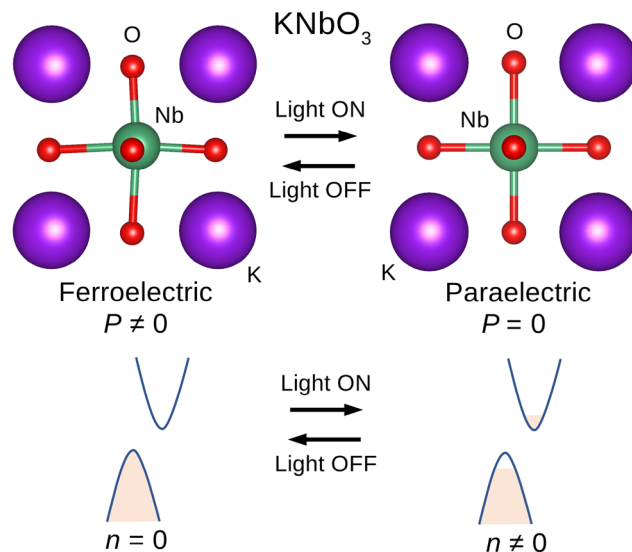

Fig. 1 Photoinduced phase transition in the perovskite oxide KNbO$_3$. The ground state is a polar rhombohedral phase (space group $R3m$). Upon photoexcitation, electrons are promoted to the conduction band ($n \neq 0$) and KNO transforms into a nonpolar cubic phase (space group $Pm\bar{3}m$), due to the screening of electrostatic dipole–dipole interactions. An analogous photoinduced phase transition occurs in the polar orthorhombic phase (space group $Amm2$) stabilized at $T \geq 225$ K.

paraelectric KNO estimated at five different conduction electron densities. Let us also note that the cell volume of the paraelectric phase slightly expands under photoexcitation (*e.g.*, the lattice parameter increases from 4.019 Å at $n = 0$ to 4.028 Å at $\bar{n}$). This is the likely reason for the generalized softening of the phonon spectrum observed with increasing n that particularly affects the high frequency region.

At a temperature of ≈225 K, KNO transforms into a polar orthorhombic phase (space group $Amm2$) that is stable up to $T \approx 493$ K.[32] For this phase, we estimated at zero temperature a 5-atom cell defined by $a = 3.996$ Å, $b = c = 4.053$ Å, $\alpha = 90.182°$, and $\beta = \gamma = 90°$, and a ferroelectric polarization of $P = 38.53$ μC cm^{-2} along the pseudocubic direction [011], which are again in very good agreement with the corresponding experimental values 3.973 Å, 4.098 Å and ≈40 μC cm^{-2}.[32,33] At zero temperature, the phonon spectrum of this phase exhibits several imaginary frequencies, indicating dynamical instability against a distortion taking the system to the rhombohedral ground state. Nevertheless, by performing phonon calculations that take the effect of temperature into account, it is possible to obtain well-behaved dispersion curves that are consistent with the experimentally observed stability of the $Amm2$ phase (see Methods, ESI Fig. 3, and Table 1:† our T-renormalized phonon calculations were performed with two different approaches, namely, normal-mode-decomposition methods[36] and QSCAILD,[37,38] that provided identical results). Interestingly, in this polar orthorhombic phase, it is also possible to stabilize the paraelectric cubic phase by means of photoexcitation; hence, we also considered it in our subsequent thermal conductivity study. The underlying mechanism is analogous to the
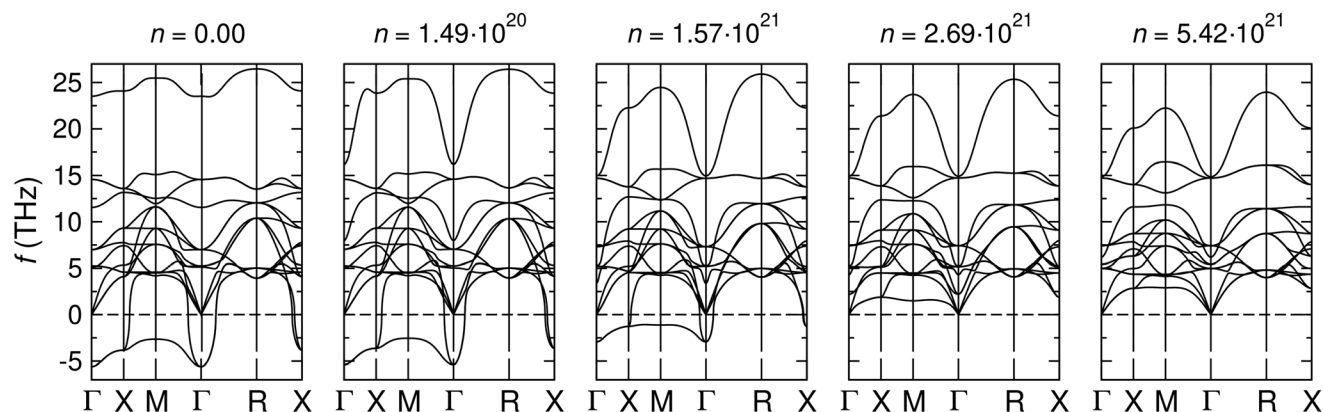
Fig. 2 Phonon dispersion of KNO in the nonpolar cubic phase for different photoexcited carrier densities. Photoexcited carrier densities were obtained by smearing the Fermi distribution with widths equal to 0.01, 0.10, 0, 30, 0.50, and 0.70 eV (left to right); n is expressed in units of conduction electrons per cm^3.

case discussed above (*i.e.*, screening of dipole–dipole interactions by photoexcited carriers). It is worth stressing that both the polar rhombohedral and orthorhombic phases spontaneously relax into the paraelectric cubic phase under sufficiently high light irradiation (or, equivalently, density of photoexcited electron–hole pairs), so they are unstable, rather than metastable, under such conditions. All phonon dispersion relations are shown in ESI Fig. 1–3.†

Let us note that photoinduced ferroelectric-to-paraelectric phase transitions analogous to those reported here for KNO have been recently predicted for $BaTiO_3$.[31] Remarkably, in the same material, the ferroelectric instability can also be suppressed by means of impurity doping, as has been theoretically and experimentally demonstrated.[39–41] In this case, electrons are injected into the conduction band from impurity states rather than promoted from the valence band *via* photoexcitation. Our DFT calculations explicitly reproduce this behavior in KNO as well.

2.2 Thermal conductivity and photophononic coupling

In what follows, we analyze the thermal conductivity changes that accompany the two photoinduced phase transitions: $R3m \rightarrow Pm\bar{3}m$ (at temperatures below 225 K, when the rhombohedral phase is observed to be stable) and $Amm2 \rightarrow Pm\bar{3}m$ (at and near room temperature, when the orthorhombic phase is observed to be stable). We compute the thermal conductivity of the different phases as specified in ESI Table 1.† Our results, expressed as a function of temperature, are shown in Fig. 3, where we plot the diagonal elements of the heat conductivity tensor along the two independent pseudocubic directions separately. A very rich scenario emerges from these plots, in which both the size and sign of κ change depend on the direction and phase transition involved. Of special interest is the κ_{xx} reduction of $\approx$30% that can be achieved at room temperature upon the light-induced $Amm2 \rightarrow Pm\bar{3}m$ phase transition. This large heat conductivity change could be exploited in various applications, such as thermal logic,[8,42] solid-state
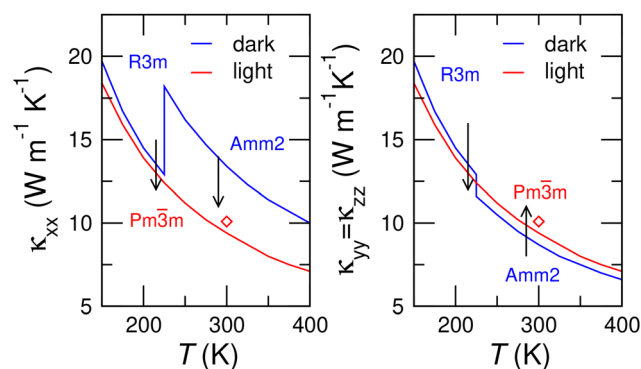
Fig. 3 Thermal conductivity of KNO along the three Cartesian axes expressed as a function of temperature. Results are shown for the ferroelectric ground state ($R3m$ at $T \leq 225$ K and $Amm2$ at $T \geq 225$ K) and the light-stabilized cubic nonpolar phase ($Pm\bar{3}m$). Arrows indicate the sign of the photoinduced κ shifts: up is positive and down is negative. The diamonds in the figure represent the room-temperature κ estimated for the cubic nonpolar phase when that is stabilized by increasing temperature under dark conditions (see the main text). See ESI Table 1† for a summary of the details of the calculation of κ in the different phases.

refrigeration[5,6] and waste heat scavenging.[7] We also tested the effect of considering room-temperature renormalized phonons (see the ESI†) in the calculation of the thermal conductivity of the light-stabilized cubic phase. We obtained a slightly larger value of κ and thus the photoswitching ratio of the $Amm2 \rightarrow Pm\bar{3}m$ transition decreases to 20%. However, this effect is most likely overestimated since we are not taking into account the thermal expansion of the material, which certainly would compensate for the aforementioned thermal conductivity increase. On the other hand, the κ changes accompanying the photoinduced $R3m \rightarrow Pm\bar{3}m$ phase transition at low temperatures are modest ($\approx$5%). It should be noted that the cubic phase is thermodynamically unstable under dark conditions, thus – disregarding possible hysteresis effects – the low conductivity state can only be accessed when light is shone on the material. Therefore, our prediction is that, when light is turned off,

reverse paraelectric-to-ferroelectric transitions occur spontaneously. Note also that a critical parameter is the light penetration depth, Δz, which in the case of being too small could result in a limiting factor for practical applications. Fortunately, from the optical absorption data reported by Kaifu and coworkers[43] we could estimate $\Delta z \approx 30$ μm, which safely exceeds the typical thickness of thin films (~10–100 nm).

It is worth noting that the anisotropy of the thermal conductivity tensor in each phase can be understood in terms of symmetry and electric polarization arguments. In the $R3m$ and $Pm\bar{3}m$ phases, the three diagonal κ components are equal along the three pseudocubic directions, just like their electric polarization components (null in the case of the cubic phase). On the other hand, in the $Amm2$ phase, it is found that $\kappa_{xx} > \kappa_{yy} = \kappa_{zz}$. In this latter case, the equivalence between the yy and zz components also follows from the orientation of the corresponding electric polarization, [011], while the difference in the xx component value can be explained by the fact that there is a mirror plane along the corresponding direction[13,15,44] (and thus the projection of the electric polarization along the x direction is null).

The two photoinduced phase transitions analyzed here involve a volume reduction of ~1%, which taken alone has a non-negligible effect on the phonon frequencies and velocities. Nevertheless, it is not always possible to rationalize the changes in the thermal conductivity based exclusively on volume changes.[45] A volume reduction, for instance, can lead to an overall hardening of the phonon frequencies, through shortening of the interatomic bonds, and thus to an increase in phonon velocities: both these factors should result in an increase of κ. Conversely, the phonon population decreases as a consequence of the increase of phonon frequencies, which should lead to lower values of κ.

A simple and effective way to ascertain the role of harmonic effects on the thermal conductivity, and thus their effect on its relative change upon the photoinduced phase transitions analyzed here, is based on the estimation of the thermal conductivity in the small-grain limit.[46] In this type of calculation, the thermal conductivity is factorized into a product of two terms. One of them is an effective global mean free path for phonons, λ, which captures the anharmonic effects. The other, κ^{SG}, is a proportionality coefficient depending only on the phonon frequencies and group velocities, both harmonic properties. λ can only be interpreted as a true uniform mean free path in a highly idealized model of a nanograined crystal in which phonon transport is limited by the grain size. In a more general setting, it is a global proxy for the intensity of phonon scattering per unit length, which in a single crystal is dominated by anharmonicity. Fig. 4 compares the κ shifts obtained in the full calculation and under the small-grain approximation for the two photoinduced polar → nonpolar phase transitions analyzed in this work. As can be appreciated therein, there is a clear contrast between both sets of data. Even at the qualitative level, the overall $\Delta\kappa_{xx}$ trend is not correctly reproduced by $\Delta\kappa_{xx}^{SG}$, while in the case of $\Delta\kappa_{yy}$ and $\Delta\kappa_{zz}$,
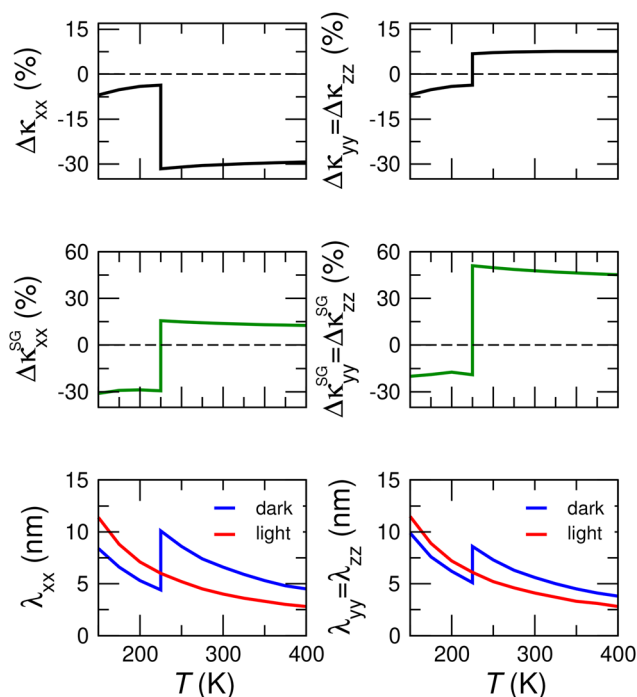

Fig. 4 Thermal conductivity variations in KNO upon the light-induced polar → nonpolar phase transformation. (Top) Directly deduced from Fig. 3. (Middle) Considering a uniform phonon mean free path of 1 nm (small-grain approximation). (Bottom) Effective global phonon mean free path, λ, computed as κ/κ^{SG}.

the small-grain limit considerably overestimates the variations. These results indicate that the changes in the thermal conductivity across the phase transitions are mostly driven by anharmonic effects (particularly for $\Delta\kappa_{xx}$ since a prediction based on κ^{SG} alone would be qualitatively incorrect). We can quantify that influence by plotting $\lambda = \kappa/\kappa^{SG}$ (Fig. 4). These results account for the phase and temperature trends obtained for $\Delta\kappa_{xx}$ – the largest variation of the κ tensor –, which was not even qualitatively captured by the small-grain model (i.e., solely based on harmonic effects).

To gain closer insight into the phonon–phonon anharmonic scattering, we first analyze the phonon phase space, Φ, which measures the number of three-phonon processes allowed by the conservation of energy and momentum. With all other factors being equal, the larger Φ is, the more likely the resistive collision processes are to occur; hence, this quantity is normally negatively correlated with the lattice thermal conductivity.[47] The $\Phi(\omega)$ results shown in Fig. 5 reveal very similar phonon phase space features for the three analyzed crystalline phases, with that corresponding to the cubic phase slightly exceeding the others. This finding is quantitatively confirmed by the insets in the same figure: the Φ_{rhom}/Φ_{cub} and Φ_{ortho}/Φ_{cub} ratios are close to unity, but smaller at all frequencies. These results can be understood by noting that the phonon phase space is essentially reflecting the unit cell complexity; the three phases involved, despite presenting different symmetries, are all described by 5-atom primitive cells; hence,
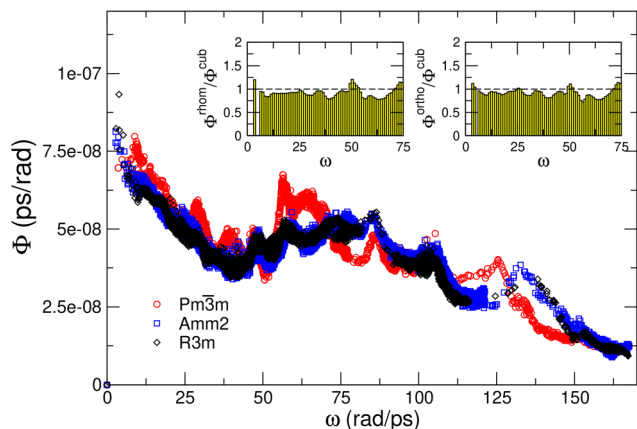
Fig. 5 Phase space of three-phonon processes allowed by the conservation of energy and momentum in KNO. Results are expressed as a function of phonon frequency and the insets show the phase space ratio for the polar and nonpolar phases considered in this study.

their respective three-phonon collision spaces turn out to be very similar. It is worth noting that in principle one could expect the Φ of the more symmetric cubic phase to be smaller. However, a larger number of nondegenerate phonon bands in the less symmetric phase does not necessarily imply a larger number of allowed phonon collision processes and thus larger Φ. Consequently, we may conclude that the thermal conductivity shifts shown in Fig. 3 are in part caused by differences in the phase space of three-phonon processes.

Next, we analyze the degree of anharmonicity of the different phases in terms of another relevant aspect, namely, the phonon scattering matrix elements. Fig. 6 shows the differences in the phonon lifetime, τ, of the polar and nonpolar phases averaged over frequency intervals of 1 rad ps^{-1}. In the two cases considered here, that is, $R3m \rightarrow Pm\bar{3}m$ at 225 K and $Amm2 \rightarrow Pm\bar{3}m$ at 300 K, the phonon lifetimes of the polar phases are noticeably longer than those of the light-stabilized nonpolar phase at most frequencies. Remarkably, there is a
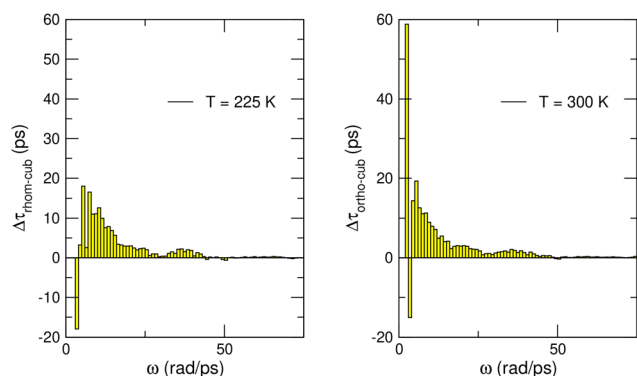
Fig. 6 Phonon lifetimes of the polar and nonpolar phases of KNO expressed as a function of phonon frequency. $\Delta\tau_{x-cub} \equiv \tau_x - \tau_{cub}$ results are averaged over frequency intervals of 1 rad ps^{-1} and correspond to $R3m \rightarrow Pm\bar{3}m$ at 225 K and $Amm2 \rightarrow Pm\bar{3}m$ at 300 K.

low-frequency range in which the phonon lifetimes of the room-temperature $Amm2$ phase are about 60 ps higher than those of the photostabilized $Pm\bar{3}m$ phase. These giant τ differences are the main cause of the largest thermal conductivity variations reported in Fig. 3 (i.e., $\Delta\kappa_{xx} \approx -30\%$ at room temperature). At temperatures below 225 K, the estimated $\Delta\tau$'s are not as large but still substantial (e.g., ~15 ps at low frequencies), which accounts for the estimated $\Delta\kappa_{xx} \approx -5\%$ (Fig. 3). The phonon lifetimes depend on the number of anharmonic scattering processes, which we quantified by the phase space, Φ, and the magnitude of the phonon–phonon anharmonic couplings. The slightly larger Φ of the cubic phase appears to be an important driving factor. It is more difficult to ascertain the role of the anharmonic couplings because of the rather similar force constants. Yet, the computed Grüneisen parameter, usually considered as a good proxy of a system's anharmonicity, suggests a certain level of synergy with the phase space (see ESI Fig. 4†), i.e., the cubic phase has a larger Φ and larger anharmonic couplings.

Electron–phonon scattering is not included in our lattice thermal conductivity calculations. It should however be noted that this additional source of scattering could only play a relevant role in the light-stabilized cubic phase, where mobile charges are present in the conduction band, further decreasing its thermal conductivity and enhancing the effect of illumination. This means that the κ change that we estimate is a lower bound of the actual value.

2.3 Cubic phase stabilized by temperature

A valid question at this stage is whether the light-stabilized cubic phase is qualitatively different from the usual cubic phase stabilized by temperature. To answer this point, we carried out T-renormalized phonon and κ calculations for the centrosymmetric phase at 300 and 800 K. In these calculations, we constrained the volume of the system to that of the light-stabilized cubic phase, allowing for direct comparisons. The results obtained are very interesting for several reasons. Firstly, at 300 K, we get rid of the dynamical instability of the cubic phase under dark conditions, namely, all its phonon branches are well-behaved (Fig. 7). In principle, this phase is experimentally not accessible since the orthorhombic $Amm2$ phase is the most stable at that temperature. However, according to our simulations the centrosymmetric phase is metastable, rather than being unstable, at $T = 300$ K; consequently, it is physically meaningful to compare the κ of the different cubic phases stabilized by either light or temperature. Secondly, the results obtained at $T = 800$ K are of practical relevance since at that temperature KNO is stable in the $Pm\bar{3}m$ phase.

Fig. 7 shows the phonon dispersions and phonon lifetimes of centrosymmetric KNO stabilized by either light or temperature. As can be appreciated therein, the two systems at room temperature are remarkably similar: not only the phonon dispersions, but also the frequency resolved lifetimes and thermal conductivities, 9.37 vs. 10.10 W m^{-1} K^{-1}, are nearly identical. These results suggest that, for all practical effects of interest here, the ferroelectric-to-paraelectric phase transition
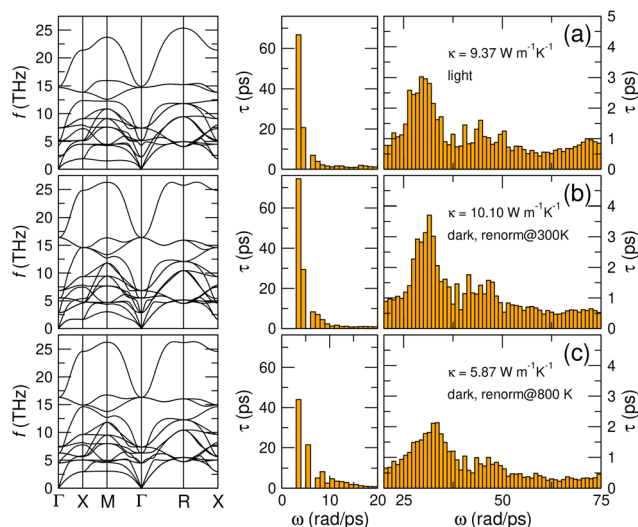
Fig. 7 Phonon dispersions and lifetimes of the cubic phase. Phonon dispersions and lifetimes averaged over frequency intervals of 1 rad ps^{-1} for the cubic $Pm\bar{3}m$ phase stabilized by (a) photoexcitation, (b) temperature at $T = 300$ K, and (c) temperature at $T = 800$ K (the calculation conditions for each case are detailed in ESI Table 1†). In (a), phonons are computed at zero temperature, while phonon lifetimes and the thermal conductivity are calculated at 300 K by considering the corresponding phonon population at that temperature. In (b and c), phonons are explicitly computed at the target temperature by means of phonon renormalization calculations (see Methods). Low- and mid-frequency lifetimes are displayed in separate panels to improve their visualization.

remains essentially the same regardless of its driving force – either light or temperature – and underlying mechanisms. Regarding the experimentally accessible high temperature cubic phase, we estimated a relatively small thermal conductivity of 5.87 W m^{-1} K^{-1} at a temperature of 800 K, which mainly results from shorter phonon lifetimes caused by stronger phonon–phonon couplings. Nevertheless, at the qualitative level, the three computed τ distributions do not feature any major difference, with the mid-frequency region being dominated by vibrations of around 30 rad ps^{-1} and the rest of the optical phonons displaying similar relative weights.

2.4 Electronic contribution to the thermal conductivity

Up to this point, we have assumed that heat was entirely transported by phonons, that is, our κ analysis has been restricted to its lattice component. This is a standard and very reasonable assumption when dealing with non-magnetic insulators and semiconductors, since the electronic contribution to the thermal conductivity, κ_{el}, is usually negligible due to the ultra-low density of free charge carriers. KNO falls into this category because its electronic band gap for the different phases ranges from 3.1 to 3.8 eV.[32] The light-stabilized nonpolar phase, however, is different in this respect since photoexcitation partially metallizes the crystal. A non-negligible κ_{el} in the cubic phase, therefore, could diminish the large κ_{xx} reduction found at room temperature upon the light-induced orthorhombic → cubic phase transition.
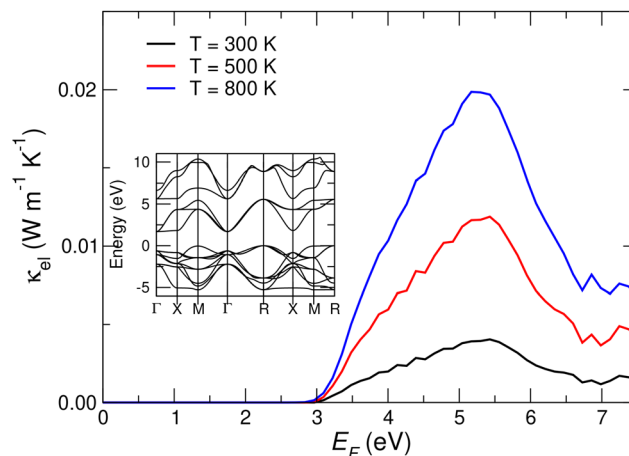
Fig. 8 Electronic thermal conductivity of KNO in the photoinduced and partially metallized cubic phase. Results are expressed as a function of electronic chemical potential, E_F (Fermi energy level), and temperature.

To assess this possibility in KNO, we explicitly computed κ_{el} for the $Pm\bar{3}m$ phase by considering electronic relaxation times obtained from *ab initio* electron–phonon coupling calculations (see Methods). Our κ_{el} results are shown in Fig. 8. It can be appreciated that, regardless of the value of the electronic chemical potential, electronic contributions to the heat conductivity are always at least two orders of magnitude smaller than those stemming from the lattice vibrations. This conclusion holds true even when considering temperatures much higher than those relevant to the present work (*i.e.*, 500 and 800 K) and is attributed to the presence of very low electronic group velocities (note the abundant flat bands in the electronic structure shown in the inset of Fig. 8). Besides the fact that κ_{el} depends quadratically on the velocities, their low values result in a high density of states near the band edges, which in turn leads to a considerable scattering of electrons.

Based on these results, we can safely neglect electronic contributions to κ for the three crystalline KNO phases considered in this study, including the light-stabilized cubic phase, since phononic heat transport is unquestionably dominant. In other materials, however, κ_{el} could be more significant in relative terms and therefore it might be necessary to take it into consideration when estimating overall thermal conductivity changes.

3 Conclusions

In conclusion, we have theoretically demonstrated light-driven dynamical tuning of the heat conductivity in KNbO$_3$, a prototypical perovskite oxide exhibiting soft-mode-driven ferroelectric phase transitions. We predicted that it is possible to induce polar to non-polar phase transitions in this material upon photoexcitation and that such transformations may entail a large decrease in κ, *e.g.* about 30% at room temperature. Interestingly, the originating phase transition mecha-

nisms, namely, photoinduced screening of the dipole–dipole interactions in the ferroelectric phases and consequent stabilization of a paraelectric phase, are operative within ample temperature intervals extending over several hundreds of kelvin. The superior heat conductivity estimated for the polar phases can be traced back to a lower level of phonon–phonon scattering resulting from weaker phonon–phonon anharmonic couplings and smaller phase space.

Analogous photophononic effects are expected to occur in other akin ferroelectric materials as well (*e.g.*, $BaTiO_3$), thus opening new avenues for the realization of innovative thermal logic, solid-state refrigeration and waste heat scavenging applications.

4 Methods

4.1 Density functional calculations

We performed density functional theory (DFT) calculations with the VASP code[48] and projector augmented waves[49,50] with an energy cutoff of 520 eV and the generalized-gradient approximation PBEsol.[51] The following electrons were explicitly treated as valence electrons: K $4s^13p^63s^2$, Nb $4d^45s^14p^6$, and O $2s^22p^4$. The Brillouin zone was sampled with a $12 \times 12 \times 12$ k-point grid and the atomic positions were optimized until all the atomic forces were smaller than 0.005 eV $Å^{-1}$. All the phases were described by 5-atom unit cells. Electric polarizations were calculated with the Born effective charge method.[52]

The second-order interatomic force constants were computed by finite differences with Phonopy[53] in $5 \times 5 \times 5$ supercells for the $R3m$ and $Amm2$ phases, while we used $4 \times 4 \times 4$ supercells for the $Pm\bar{3}m$ phase. Non-analytical corrections proved to induce contamination of the acoustic branches that led to spurious instability in the $Amm2$ phase, and thus were only included in the $R3m$ and $Pm\bar{3}m$ phases. For the third-order interatomic force constants we used thirdorder.py[54] and $3 \times 3 \times 3$ supercells with a cutoff of 4.4 Å in the three-phonon scattering processes, which spans up to the 8th nearest neighbors in the $R3m$ phase. We then solved the phonon Boltzmann transport equation (BTE) beyond the relaxation time approximation (RTA) on a $18 \times 18 \times 18$ grid of $\mathbf{q}$-points with the almaBTE code.[55] Scattering from isotopic disorder was accounted for through the model of Tamura.[56] The lattice thermal conductivity was estimated as:

$$\kappa_{ij} = \sum_\lambda C_\lambda v_{\lambda,i} F_{\lambda,j}, \tag{1}$$

where the sum runs over all phonon modes, the index λ including both the $\mathbf{q}$-point and the phonon band and where i and j run over the Cartesian directions x, y, and z. C_λ is the contribution of mode λ to the volumetric heat capacity, v is the group velocity and F_λ is a generalized mean free path.[55]

Although phonon–phonon scattering processes beyond third-order have not been considered in this study, further works should address their influence on the photophononic

effects reported here. While in general fourth-order phonon–phonon processes are relevant for situations in which three-phonon scattering is weak[57] or at high temperatures, none of which apply to the present study, those may be non-negligible in other cases as well (see *e.g.*, ref. 58 and 59).

Photoexcitation of the cubic phase was achieved by constraining the partial occupancies of each electronic orbital through adjustment of the Fermi distribution smearing, σ. For sufficiently large values of σ, the valence (conduction) band is partially emptied (filled). We estimated the density of photoexcited carriers by integrating the number of electrons in the conduction band over all k-points (see Table 1). This effective DFT approach is equivalent to those previously employed in other works.[31,60] In particular, Paillard *et al.*[31] demonstrated that, with regard to light-driven transitions and the suppression of ferroelectricity in perovskite oxides, electronic smearing correctly reproduces the results obtained with more sophisticated approaches to treat the photoexcited state. They compared the results obtained by imposing a Fermi–Dirac smearing, similarly to the present work, with those obtained by running a constrained DFT calculation with a fixed concentration of electron–hole pairs *via* the introduction of two adjustable quasi-Fermi levels. They found that the results were qualitatively the same, which justifies the use of this effective method for a proof-of-concept study as the present one.

In this scheme, charge neutrality is always preserved, as in the case of photodoping. Therefore, no compensating background must be added, thus avoiding potential artifacts that, as previously reported, can lead to spurious pressure effects.[61]

4.2 Anharmonic lattice dynamics from *ab initio* molecular dynamics simulations

The DynaPhoPy code[36] was used to calculate the anharmonic lattice dynamics of $KNbO_3$ (*e.g.*, T-renormalized phonons) from *ab initio* molecular dynamics (AIMD) simulations. To this end, a normal-mode-decomposition technique was employed in which the atomic velocities $v_{jl}(t)$ (j and l represent particle and Cartesian direction indexes) generated during fixed-temperature AIMD simulation runs were expressed as:

$$\mathbf{v}_{jl}(t) = \frac{1}{\sqrt{Nm_j}} \sum_{\mathbf{q}s} e_j(\mathbf{q}, s) e^{i\mathbf{q}R_{jl}^0} v_{\mathbf{q}s}(t), \tag{2}$$

Table 1 Photoexcited charge density in $Pm\bar{3}m$ KNO for different values of smearing applied on the Fermi–Dirac occupation distribution

σ	n [cm^{-3}]
0.10	2.02×10^{18}
0.20	1.49×10^{20}
0.30	6.91×10^{20}
0.40	1.57×10^{21}
0.50	2.69×10^{21}
0.60	3.99×10^{21}
0.70	5.42×10^{21}
0.80	6.96×10^{21}
0.90	8.57×10^{21}
1.00	1.02×10^{22}

where N is the number of particles, m_j is the mass of particle j, $e_j(\mathbf{q}, s)$ is a phonon mode eigenvector ($\mathbf{q}$ and s stand for the wave vector and phonon branch), R_{jl}^0 is the equilibrium position of particle j, and $v_{\mathbf{q}s}$ is the velocity of the corresponding phonon quasiparticle. The Fourier transform of the autocorrelation function of $v_{\mathbf{q}s}$ was then calculated, yielding the power spectrum:

$$G_{\mathbf{q}s}(\omega) = 2 \int_{-\infty}^{\infty} \left\langle v_{\mathbf{q}s}^*(0) v_{\mathbf{q}s}(t) \right\rangle e^{i\omega t} \mathrm{d}t. \tag{3}$$

Finally, this power spectrum was approximated by a Lorentzian function of the form:

$$G_{\mathbf{q}s}(\omega) \approx \frac{\left\langle |v_{\mathbf{q}s}|^2 \right\rangle}{\frac{1}{2}\gamma_{\mathbf{q}s}\pi\left[1 + \left(\frac{\omega - \omega_{\mathbf{q}s}}{\frac{1}{2}\gamma_{\mathbf{q}s}}\right)^2\right]}, \tag{4}$$

from which a T-renormalized quasiparticle phonon frequency, $\omega_{\mathbf{q}s}(T)$, was determined as the peak position and the corresponding phonon linewidth, $\gamma_{\mathbf{q}s}(T)$, as the full width at half maximum.

AIMD simulations based on DFT (performed with the VASP code) were carried out in the (N, V, T) ensemble for bulk $KNbO_3$ in the orthorhombic phase at a temperature of 300 K. The selected volume was that of equilibrium determined at zero temperature; hence, thermal expansion effects were neglected. The temperature in the AIMD simulations was kept fluctuating around a set-point value by using Nosé–Hoover thermostats. A large simulation cell containing $N = 625$ atoms was employed with periodic boundary conditions applied along the three Cartesian directions. Newton's equations of motion were integrated by using the customary Verlet's algorithm and a time-step length of 15^{-3} ps. Γ-point sampling for integration within the first Brillouin zone was employed and the total duration of the AIMD simulations was 40 ps.

4.3 Self-consistent finite-temperature phonon calculations

An adapted version of the QSCAILD method,[37] as introduced in ref. 38, is used to calculate finite-temperature phonon spectra through effective harmonic potentials. Using the eigenvectors, $e_j(\mathbf{q},s)$, and -values, $\omega_{\mathbf{q}s}$, of the finite-displacement force constants corresponding to the first trial potential, $\mathcal{V}$, a trial density matrix, ρ, is constructed as a function of mass-weighted displacements $u_{jl} = m_j^{-1/2}(R_{jl} - R_{jl}^0)$:

$$\rho(u) = \frac{1}{\sqrt{(2\pi)^{3N}|C|}} \exp\left(-\frac{1}{2}u^T C^{-1} u\right). \tag{5}$$

The blocks of the covariance matrix, C, are obtained as

$$C_{ij} = \frac{\hbar}{2\sqrt{m_i m_j}} \sum_{\mathbf{q}s} \frac{1}{\omega_{\mathbf{q}s} \tanh\frac{\hbar\omega_{\mathbf{q}s}}{2k_\mathrm{B}T}} e_i(\mathbf{q},s) \otimes e_j(\mathbf{q},s)^*, \tag{6}$$

using a temperature of $T = 300$ K. At each iteration, 5 displaced structures are sampled from ρ, their energies and forces are obtained through DFT in a $5 \times 5 \times 5$ supercell at Γ, and a new trial potential is built through a minimization procedure.

Symmetries are properly accounted for through the use of hiPhive[62] with a cutoff of $r_\mathrm{c} = 9.9$ Å. From there, the next iteration density matrix is built through Pulay mixing[63] with a mixing parameter of $\alpha = 0.2$ and a memory of $l = 5$ steps. Subsequent steps include having all the structures obtained to this point reweighted according to the originating and current density matrices. This procedure is repeated until the free energy,

$$\begin{aligned} \mathcal{F}(T) = \sum_{\mathbf{q}s} \left(\frac{\hbar\omega_{\mathbf{q}s}}{2} + k_\mathrm{B}T \log\left[1 - \exp\left\{-\frac{\hbar\omega_{\mathbf{q}s}}{k_\mathrm{B}T}\right\}\right]\right) \\ + \frac{1}{N}\sum_n (E_n - \tilde{E}_n), \end{aligned} \tag{7}$$

is converged to within 2.5 meV per atom. In eqn (7), the first term corresponds to the harmonic free energy and the latter to a weighted average of the differences between the DFT-calculated energies, E, and the approximate energies obtained through the $\mathcal{V}$, for each of the N structures.

4.4 Electron–phonon scattering calculations

We use the electron–phonon averaged approximation (EPA)[64] to treat electron scattering by phonons, the main mechanism determining the electronic lifetime. Under that approximation, electron–phonon matrix elements are averaged over wave vectors, resulting in an energy-dependent contribution to the electronic scattering rates.

We use the reference software implementation of the EPA in combination with BoltzTraP2.[65] We run the required DFT calculations with Quantum ESPRESSO[66] employing ultrasoft pseudopotentials, charge-density and wave-function plane-wave cutoffs of 600 and 75 Ry, respectively, a Fermi–Dirac smearing parameter matching the VASP calculations and an 11 × 11 × 11 k-point grid that is later non-self-consistently refined to 32 × 32 × 32.

Conflicts of interest

There are no conflicts to declare.

Acknowledgements

References

1 R. Gurunathan, R. Hanus and G. J. Snyder, *Mater. Horiz.*, 2020, **7**, 1452–1456.

2 M. Sledzinska, R. Quey, B. Mortazavi, B. Graczykowski, M. Placidi, D. Saleta Reig, D. Navarro-Urrios, F. Alzina, L. Colombo, S. Roche and C. M. Sotomayor Torres, *ACS Appl. Mater. Interfaces*, 2017, **9**, 37905–37911.

3 N. Mingo, L. Yang, D. Li and A. Majumdar, *Nano Lett.*, 2003, **3**, 1713–1716.

4 M. Maldovan, *Nat. Mater.*, 2015, **14**, 667–674.

5 R. I. Epstein and K. J. Malloy, *J. Appl. Phys.*, 2009, **106**, 064509.

6 Y. Jia and Y. Sungtaek Ju, *Appl. Phys. Lett.*, 2012, **100**, 242901.

7 G. Wehmeyer, T. Yabuki, C. Monachon, J. Wu and C. Dames, *Appl. Phys. Rev.*, 2017, **4**, 041304.

8 N. Li, J. Ren, L. Wang, G. Zhang, P. Hänggi and B. Li, *Rev. Mod. Phys.*, 2012, **84**, 1045–1066.

9 M. Maldovan, *Nature*, 2015, **14**, 209–217.

10 K. Nakagawa, K. Satoh, S. Murakami, K. Takei, S. Akita and T. Arie, *Sci. Rep.*, 2021, **11**, 19533.

11 A. Sood, F. Xiong, S. Chen, H. Wang, D. Selli, J. Zhang, C. J. McClellan, J. Sun, D. Donadio, Y. Cui, E. Pop and K. E. Goodson, *Nat. Commun.*, 2018, **9**, 4510.

12 G. Qin, Z. Qin, S.-Y. Yue, Q.-B. Yan and M. Hu, *Nanoscale*, 2017, **9**, 7227–7234.

13 J. A. Seijas-Bellido, H. Aramberri, J. Íñiguez and R. Rurali, *Phys. Rev. B*, 2018, **97**, 184306.

14 P. Torres, J. A. Seijas-Bellido, C. Escorihuela-Sayalero, J. Íñiguez and R. Rurali, *Phys. Rev. Mater.*, 2019, **3**, 044404.

15 P. Torres, J. Íñiguez and R. Rurali, *Phys. Rev. Lett.*, 2019, **123**, 185901.

16 C. Liu, Y. Chen and C. Dames, *Phys. Rev. Appl.*, 2019, **11**, 044002.

17 Z. Yang, K. Yuan, J. Meng and M. Hu, *Nanoscale*, 2020, **12**, 19178–19190.

18 C. Cazorla and R. Rurali, *Phys. Rev. B*, 2022, **105**, 104401.

19 C. Cazorla, M. Stengel, J. Íñiguez and R. Rurali, *npj Comput. Mater.*, 2023, **9**, 97.

20 N. Varela-Domínguez, C. López-Bueno, A. López-Moreno, M. S. Claro, G. Rama, V. Leborán, M. d. C. Giménez-López and F. Rivadulla, *J. Mater. Chem. C*, 2023, **11**, 4588–4594.

21 K. Nasu, H. Ping and H. Mizouchi, *J. Phys.: Condens. Matter*, 2001, **13**, R693.

22 S. Koshihara, *J. Phys.: Conf. Ser.*, 2005, **21**, 7.

23 S. Koshihara, Y. Tokura, K. Takeda and T. Koda, *Phys. Rev. Lett.*, 1992, **68**, 1148–1151.

24 A. Cavalleri, C. Tóth, C. W. Siders, J. A. Squier, F. Ráksi, P. Forget and J. C. Kieffer, *Phys. Rev. Lett.*, 2001, **87**, 237401.

25 F. O. Karutz, J. U. von Schütz, H. Wachtel and H. C. Wolf, *Phys. Rev. Lett.*, 1998, **81**, 140–143.

26 A. Zong, A. Kogar, Y.-Q. Bie, T. Rohwer, C. Lee, E. Baldini, E. Ergeçen, M. B. Yilmaz, B. Freelon, E. J. Sie, H. Zhou, J. Straquadine, P. Walmsley, P. E. Dolgirev, A. V. Rozhkov, I. R. Fisher, P. Jarillo-Herrero, B. V. Fine and N. Gedik, *Nat. Phys.*, 2019, **15**, 27–31.

27 M. S. Kirschner, B. T. Diroll, P. Guo, S. M. Harvey, W. Helweh, N. C. Flanders, A. Brumberg, N. E. Watkins, A. A. Leonard, A. M. Evans, M. R. Wasielewski, W. R. Dichtel, X. Zhang, L. X. Chen and R. D. Schaller, *Nat. Commun.*, 2019, **10**, 504.

28 V. Krapivin, M. Gu, D. Hickox-Young, S. W. Teitelbaum, Y. Huang, G. de la Peña, D. Zhu, N. Sirica, M.-C. Lee, R. P. Prasankumar, A. A. Maznev, K. A. Nelson, M. Chollet, J. M. Rondinelli, D. A. Reis and M. Trigo, *Phys. Rev. Lett.*, 2022, **129**, 127601.

29 K. Iwano, Y. Shimoi, T. Miyamoto, D. Hata, M. Sotome, N. Kida, S. Horiuchi and H. Okamoto, *Phys. Rev. Lett.*, 2017, **118**, 107404.

30 T. Yang, C. Dai and L.-Q. Chen, *Nano Lett.*, 2023, **23**, 2551–2556.

31 C. Paillard, E. Torun, L. Wirtz, J. Íñiguez and L. Bellaiche, *Phys. Rev. Lett.*, 2019, **123**, 087601.

32 D. Wang, G. Wang, Z. Lu, Z. Al-Jlaihawi and A. Feteira, *Front. Mater.*, 2020, **7**, 91.

33 A. I. Frenkel, F. M. Wang, S. Kelly, R. Ingalls, D. Haskel, E. A. Stern and Y. Yacoby, *Phys. Rev. B: Condens. Matter Mater. Phys.*, 1997, **56**, 10869–10877.

34 M. D. Fontana, G. Metrat, J. L. Servoin and F. Gervais, *J. Phys. C: Solid State Phys.*, 1984, **17**, 483.

35 R. E. Cohen, *Nature*, 1992, **358**, 136–138.

36 A. Carreras, A. Togo and I. Tanaka, *Comput. Phys. Commun.*, 2017, **221**, 221–234.

37 A. van Roekeghem, J. Carrete and N. Mingo, *Comput. Phys. Commun.*, 2021, **263**, 107945.

38 S. Bichelmaier, J. Carrete, M. Nelhiebel and G. K. H. Madsen, *Phys. Status Solidi RRL*, 2022, **16**, 2100642.

39 Y. Wang, X. Liu, J. D. Burton, S. S. Jaswal and E. Y. Tsymbal, *Phys. Rev. Lett.*, 2012, **109**, 247601.

40 H. J. Zhao, A. Filippetti, C. Escorihuela-Sayalero, P. Delugas, E. Canadell, L. Bellaiche, V. Fiorentini and J. Íñiguez, *Phys. Rev. B*, 2018, **97**, 054107.

41 J. Fujioka, A. Doi, D. Okuyama, D. Morikawa, T. Arima, K. N. Okada, Y. Kaneko, T. Fukuda, H. Uchiyama, D. Ishikawa, A. Q. R. Baron, K. Kato, M. Takata and Y. Tokura, *Sci. Rep.*, 2015, **5**, 13207.

42 L. Wang and B. Li, *Phys. Rev. Lett.*, 2007, **99**, 177208.

43 Y. Kaifu, T. Komatsu, T. Hirano and T. Inoguchi, *J. Phys. Soc. Jpn.*, 1967, **23**, 903–903.

44 J. A. Seijas-Bellido, I. J. Íñiguez and R. Rurali, *Appl. Phys. Lett.*, 2019, **115**, 192903.

45 L. Lindsay, D. A. Broido, J. Carrete, N. Mingo and T. L. Reinecke, *Phys. Rev. B: Condens. Matter Mater. Phys.*, 2015, **91**, 121202(R).

46 J. Carrete, W. Li, N. Mingo, S. Wang and S. Curtarolo, *Phys. Rev. X*, 2014, **4**, 011019.

47 L. Lindsay and D. A. Broido, *J. Phys.: Condens. Matter*, 2008, **20**, 165209.

48 G. Kresse and J. Furthmüller, *Phys. Rev. B: Condens. Matter Mater. Phys.*, 1996, **54**, 11169.

49 P. E. Blöchl, *Phys. Rev. B: Condens. Matter Mater. Phys.*, 1994, **50**, 17953.

50 G. Kresse and D. Joubert, *Phys. Rev. B: Condens. Matter Mater. Phys.*, 1999, **59**, 1758.

51 J. P. Perdew, A. Ruzsinszky, G. I. Csonka, O. A. Vydrov, G. E. Scuseria, L. A. Constantin, X. Zhou and K. Burke, *Phys. Rev. Lett.*, 2008, **100**, 136406.

52 C. Menéndez and C. Cazorla, *Phys. Rev. Lett.*, 2020, **125**, 117601.

53 A. Togo and I. Tanaka, *Scr. Mater.*, 2015, **108**, 1–5.

54 W. Li, J. Carrete, N. A. Katcho and N. Mingo, *Comput. Phys. Commun.*, 2014, **185**, 1747–1758.

55 J. Carrete, B. Vermeersch, A. Katre, A. van Roekeghem, T. Wang, G. K. Madsen and N. Mingo, *Comput. Phys. Commun.*, 2017, **220**, 351–362.

56 S. Tamura, *Phys. Rev. B: Condens. Matter Mater. Phys.*, 1983, **27**, 858–866.

57 A. Kundu, X. Yang, J. Ma, T. Feng, J. Carrete, X. Ruan, G. K. H. Madsen and W. Li, *Phys. Rev. Lett.*, 2021, **126**, 115901.

58 Y. Zhao, S. Zeng, G. Li, C. Lian, Z. Dai, S. Meng and J. Ni, *Phys. Rev. B*, 2021, **104**, 224304.

59 J. Zheng, D. Shi, Y. Yang, C. Lin, H. Huang, R. Guo and B. Huang, *Phys. Rev. B*, 2022, **105**, 224303.

60 B. Peng, Y. Hu, S. Murakami, T. Zhang and B. Monserrat, *Sci. Adv.*, 2020, **6**, eabd1618.

61 D. Hickox-Young, D. Puggioni and J. M. Rondinelli, *Phys. Rev. Mater.*, 2023, **7**, 010301.

62 F. Eriksson, E. Fransson and P. Erhart, *Adv. Theory Simul.*, 2019, **2**, 1800184.

63 P. Pulay, *J. Comput. Chem.*, 1982, **3**, 556–560.

64 G. Samsonidze and B. Kozinsky, *Adv. Energy Mater.*, 2018, **8**, 1800246.

65 G. K. Madsen, J. Carrete and M. J. Verstraete, *Comput. Phys. Commun.*, 2018, **231**, 140–145.

66 P. Giannozzi, S. Baroni, N. Bonini, M. Calandra, R. Car, C. Cavazzoni, D. Ceresoli, G. L. Chiarotti, M. Cococcioni, I. Dabo, A. Dal Corso, S. de Gironcoli, S. Fabris, G. Fratesi, R. Gebauer, U. Gerstmann, C. Gougoussis, A. Kokalj, M. Lazzeri, L. Martin-Samos, N. Marzari, F. Mauri, R. Mazzarello, S. Paolini, A. Pasquarello, L. Paulatto, C. Sbraccia, S. Scandolo, G. Sclauzero, A. P. Seitsonen, A. Smogunov, P. Umari and R. M. Wentzcovitch, *J. Phys.: Condens. Matter*, 2009, **21**, 395502.